J. Fluid Mech. (2001), *vol.* 429, *pp.* 283–305. Printed in the United Kingdom

© 2001 Cambridge University Press

The generation of axial vorticity in solid-propellant rocket-motor flows

By S. BALACHANDAR[1], J. D. BUCKMASTER[2,1] AND M. SHORT[1]

[1]Theoretical and Applied Mechanics, University of Illinois, Urbana, IL 61801, USA
[2]Aeronautical and Astronautical Engineering, University of Illinois, Urbana, IL 61801, USA

(Received 17 May 1999 and in revised form 9 September 2000)

We examine small deviations from axial symmetry in a solid-propellant rocket motor, and describe a 'bath-tub-vortex' effect, in which substantial axial vorticity is generated in a neighbourhood of the chamber centreline. The unperturbed flow field is essentially inviscid at modest Reynolds numbers, even at the chamber walls, as has long been known, but the inviscid perturbed flow is singular at the centreline, and viscous terms are required to regularize it. We examine perturbations sufficiently small that a linear analysis is valid everywhere (εRe small, where ε is a measure of the perturbation amplitude and Re is a Reynolds number), and larger perturbations in which a nonlinear patch is created near the centreline of radius $O(\sqrt{\varepsilon})$. Our results provide an explanation of swirl experimentally observed by others, and a cautionary note for those concerned with numerical simulations of these flows, whether laminar or turbulent.

1. Introduction

It has been known since the pioneering work of Taylor (1956) that interior flows generated by a flux at the boundary can (indeed must) satisfy the no-slip condition without benefit of viscosity, since the boundary layer is blown off by the injection. An important example is the flow inside a solid-propellant rocket motor, a problem that was first discussed by Culick (1966): he constructed an inviscid rotational solution for flow in a long right-circular cylinder with sidewall injection. Curiously, there has been little if any work on flows in channels with more complex cross-sections, despite the fact that solid-propellant grain configurations are seldom circular (Sutton 1992), and it is this issue that is the subject of the present paper. More precisely, we are concerned with flows that are not axisymmetric, either because the cross-section is not axisymmetric, or because of variations in the injection (burning) rate around the circumference. A grain configuration that is commonly used in rocket motors is star-shaped, and injection at the star boundary (associated with the gasification of the solid) generates a substantial azimuthal flow component. Little is known about such flows.

The general problem is not amenable to analysis, and we do not consider it here: instead, we consider perturbations of Culick's solution. We find that viscous terms cannot be neglected everywhere, although there is no boundary layer, and a linear analysis is only valid if $\varepsilon Re \ll 1$, where ε is a measure of the perturbation and Re is an appropriate Reynolds number. Otherwise a nonlinear axial patch of radius $\sim\sqrt{\varepsilon}$ exists in which the axial vorticity is $O(1)$. This vorticity is an increasing function of

https://doi.org/10.1017/S0022112000002688 Published online by Cambridge University Press

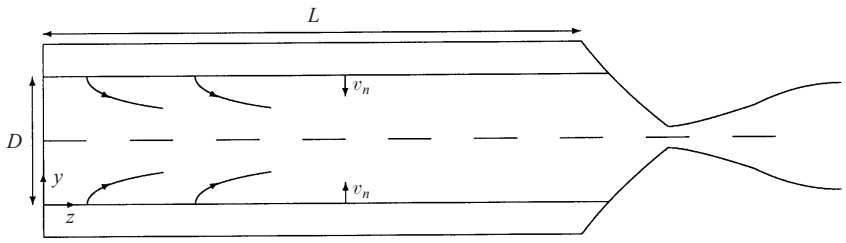


FIGURE 1. Rocket chamber configuration.

Re, with magnitude $\sim Re$ when $\varepsilon Re \gg 1$. Our general conclusion is that modest deviations from symmetry can have profound effects on the nature of the flow field.

Our analysis proceeds as follows. We show why there can be no sidewall boundary layer in a long cylinder with sidewall injection; we formulate the equations for a large-aspect-ratio cylinder; and we identify Culick's solution for a circular cross-section. We then consider small inviscid perturbations to Culick's solution and show that the axial vorticity, a perturbation quantity, is singular like $1/r^2$ as $r \to 0$. This solution can be regularized by viscous terms, important on the scale $r = O(1/\sqrt{Re})$, and in this *viscous core* the axial vorticity is $O(\varepsilon Re)$, which must be small. A complete description of the perturbation flow field is presented, both within the viscous core and in the surrounding inviscid annulus. When εRe is not small it is shown that there is a nonlinear patch on the scale $r = O(\sqrt{\varepsilon})$ embedded in the linearly perturbed inviscid flow, and that in this patch the axial vorticity is $O(1)$. Again, viscous terms are needed within a viscous core to regularize the solution as $r \to 0$, and because of this the vorticity is an unbounded function of Re. Solutions within the nonlinear patch are constructed numerically.

2. Rocket-chamber flows and blow-off of the boundary layer

A solid-propellant rocket motor consists of a chamber, lined with propellant, to which a nozzle is attached. Combustion processes in the neighbourhood of the propellant surface heat it, causing it to regress, generating voluminous quantities of gas. Because of the disparity between the gas density and the solid density, the gas velocity normal to the surface is much greater than the regression rate, so that on gas-phase time scales the flow may be modelled by flow injection from a fixed surface. That this surface cannot support a boundary layer is apparent from the following argument.

Consider the rocket chamber shown in figure 1 which, for the purposes of the immediate argument, we will suppose is two-dimensional (plane). We seek a description of the flow field in terms of the classical dichotomy of an inviscid irrotational core flow and Prandtl boundary layers. The core flow is

$$(v, w) = \frac{2v_n}{D}\left(-y + \frac{D}{2}, z\right) \tag{2.1}$$

where v_n is the wall-normal injection velocity and D is the separation distance between the top and bottom walls. Then the speed at the edge of the boundary layer on the lower wall is

$$w(z) = \frac{2v_n z}{D}, \tag{2.2}$$

as in Hiemenz flow. Unlike the classical Hiemenz configuration, however, there is a

https://doi.org/10.1017/S0022112000002688 Published online by Cambridge University Press

substantial blowing velocity and the boundary conditions at the wall are

$$(v, w) = (v_n, 0) \quad \text{at} \quad y = 0. \tag{2.3}$$

A boundary layer solution, if it existed, would be valid for values of $z \gg D$, a region well removed from endwall effects.

The inviscid solution (2.1) is characterized by a rate of strain

$$\alpha = \frac{2v_n}{D} \tag{2.4}$$

from which a characteristic speed $\sqrt{\alpha\nu}$ can be defined (ν is the kinematic viscosity), a measure of v in the Hiemenz solution (Batchelor 1967). Thus for a boundary layer solution to exist, necessarily

$$v_n \leqslant \sqrt{\alpha\nu}, \quad \text{i.e.} \quad v_n \leqslant \frac{2\nu}{D}. \tag{2.5}$$

With $\nu = 1.49 \times 10^{-3}\,\mathrm{m^2\,s^{-1}}$, a value appropriate for a temperature of 3000 K, and $D = 0.6\,\mathrm{m}$, then $2\nu/D \sim 5 \times 10^{-3}\,\mathrm{m\,s^{-1}}$ which is much smaller than a typical blowing velocity (~ 1). Indeed, a typical regression rate of the *solid* is $\sim 10^{-2}\,\mathrm{m\,s^{-1}}$. But the difficulty is not merely one identified from quantitative considerations: the length $(\nu/\alpha)^{1/2}$ is characteristic of the boundary layer thickness (Batchelor 1967), so that we require

$$\sqrt{\frac{\nu}{\alpha}} \ll \frac{D}{2}, \quad \text{i.e.} \quad v_n \gg \frac{2\nu}{D}, \tag{2.6}$$

in contradistinction with the inequality (2.5). Thus blow-off is assured. There is, of course, a large literature on the effects of strong blowing on boundary layers, e.g. Cole & Aroesty (1968).

3. Inviscid flow in a large-aspect-ratio chamber

In the absence of a boundary layer we seek rotational solutions of Eulers equations that satisfy the no-slip condition at the wall in addition to the blowing condition. Note that there is no difficulty in prescribing the values of all three velocity components at the wall where the characteristics (streamlines) enter the domain. Only if the flow were potential would this not be possible, equivalent to the simultaneous specification of Dirichlet and Neumann data for a harmonic function.

Figure 1 is still appropriate, but now cylindrical with arbitrary cross-section. Also we place the origin of the coordinate system on some appropriately chosen axis, rather than at the sidewall. We have

$$\nabla \cdot \boldsymbol{q} = 0, \quad \boldsymbol{q} \cdot \nabla \boldsymbol{q} = -\frac{1}{\rho}\nabla p, \quad \boldsymbol{q} = (u, v, w). \tag{3.1}$$

The variables are now scaled in the following fashion: u and v with v_n; w with $2v_nL/D$; x and y with $D/2$; z with L; p with $4\rho v_n^2 L^2/D^2$. Moreover we write the scaled pressure as

$$\bar{p} = P_0(z) + \frac{D^2}{4L^2}P_1 \tag{3.2}$$

and assume that $D/L \ll 1$, whence

$$\bar{\nabla} \cdot \bar{\boldsymbol{q}} = 0, \quad \bar{\boldsymbol{q}} \cdot \bar{\nabla} \begin{pmatrix} \bar{u} \\ \bar{v} \end{pmatrix} = \begin{pmatrix} -\partial P_1/\partial \bar{x} \\ -\partial P_1/\partial \bar{y} \end{pmatrix}, \quad \bar{\boldsymbol{q}} \cdot \bar{\nabla}\bar{w} = -\frac{\mathrm{d}P_0}{\mathrm{d}z}. \tag{3.3}$$

https://doi.org/10.1017/S0022112000002688 Published online by Cambridge University Press

These equations have a separable solution of the form:

$$\bar{w} = z\tilde{w}(\bar{x},\bar{y}), \quad \bar{u} = \tilde{u}(\bar{x},\bar{y}), \quad \bar{v} = \tilde{v}(\bar{x},\bar{y}), \quad P_0 = -\tfrac{1}{2}Cz^2, \quad P_1 \equiv P_1(\bar{x},\bar{y}), \tag{3.4}$$

with C a constant, whereupon (3.3) reduce to

$$\frac{\partial\tilde{u}}{\partial\bar{x}} + \frac{\partial\tilde{v}}{\partial\bar{y}} + \tilde{w} = 0, \tag{3.5a}$$

$$\tilde{u}\frac{\partial\tilde{w}}{\partial\bar{x}} + \tilde{v}\frac{\partial\tilde{w}}{\partial\bar{y}} + \tilde{w}^2 = C, \tag{3.5b}$$

$$\left(\tilde{u}\frac{\partial}{\partial\bar{x}} + \tilde{v}\frac{\partial}{\partial\bar{y}}\right)\begin{pmatrix}\tilde{u}\\ \tilde{v}\end{pmatrix} = \begin{pmatrix}-\partial P_1/\partial\bar{x}\\ -\partial P_1/\partial\bar{y}\end{pmatrix}. \tag{3.5c}$$

These equations describe the flow field for a large-aspect-ratio chamber when $z \gg D$. The boundary conditions on the chamber walls are

$$\tilde{w} = 0, \quad (\tilde{u},\tilde{v})\cdot\boldsymbol{n} = 1, \quad (\tilde{u},\tilde{v})\times\boldsymbol{n} = 0, \tag{3.6}$$

where $\boldsymbol{n}$ is the inner normal.

Our development of the asymptotic description here has been mechanical, for the ingredients are clear from an examination of Taylor's work, presented in his trademark physical style (Taylor 1956). But that the pressure to leading order is uniform across the chamber is a familiar consequence of the slenderness; and the linearity of $\bar{w}$ with z simply reflects the fact that the total amount of injected fluid which supplies the axial flow grows linearly with z when v_n is constant.

The solution for a circular cylinder of unit radius, first given by Culick (1966), is

$$\tilde{v}_r = -\frac{1}{\bar{r}}\sin(\tfrac{1}{2}\pi\bar{r}^2), \quad \tilde{w} = \pi\cos(\tfrac{1}{2}\pi\bar{r}^2), \quad C = \pi^2. \tag{3.7}$$

Note that there are no corresponding axisymmetric solutions with swirl when $\tilde{v}_\theta$ vanishes at the wall, for azimuthal momentum conservation requires

$$\tilde{v}_\theta\bar{r} = \text{const} \tag{3.8}$$

(conservation of angular momentum for the radially moving flow). Should $\tilde{v}_\theta$ not vanish at the wall, a case we discuss in § 9.1, it is apparent that $\tilde{v}_\theta$ is singular on the centreline in the inviscid context. Regularization comes from reinstating the viscous terms, a general theme in our discussion whenever there is swirl, axisymmetric or not.

It is not difficult to show that the axisymmetric equations reduce to the plane equations under the substitutions $\bar{r}\tilde{v}_r \to \tilde{v}$, $\bar{r}^2 \to \bar{y}$, $\tilde{w} \to 2\tilde{w}$, $C \to 4C$, whence the solution in the plane case is

$$\tilde{v} = -\sin(\tfrac{1}{2}\pi\bar{y}), \quad \tilde{w} = \tfrac{1}{2}\pi\cos(\tfrac{1}{2}\pi\bar{y}), \quad C = \tfrac{1}{4}\pi^2. \tag{3.9a–c}$$

Compressible counterparts to these solutions are discussed by Balakrishnan, Liñán & Williams (1991, 1992). We will not discuss compressible effects in this paper.

4. Finite Reynolds number solutions

The viscous counterparts to (3.5b, c) are

$$\tilde{u}\frac{\partial\tilde{w}}{\partial\bar{x}} + \tilde{v}\frac{\partial\tilde{w}}{\partial\bar{y}} + \tilde{w}^2 = C + \frac{1}{Re}\nabla_c^2\tilde{w}, \tag{4.1a}$$

https://doi.org/10.1017/S0022112000002688 Published online by Cambridge University Press

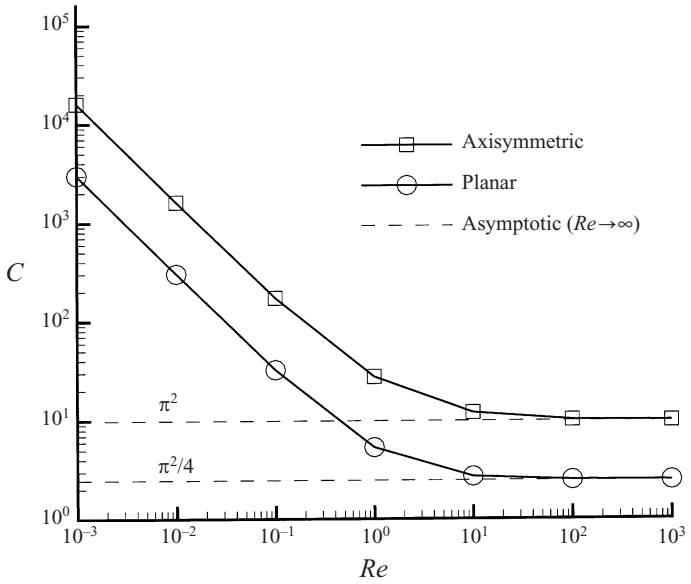


FIGURE 2. Variations of pressure gradient C with Reynolds number Re for steady viscous solutions.

$$\left(\tilde{u}\frac{\partial}{\partial\bar{x}}+\tilde{v}\frac{\partial}{\partial\bar{y}}\right)\begin{pmatrix}\tilde{u}\\ \tilde{v}\end{pmatrix}=\begin{pmatrix}-\partial P_1/\partial\bar{x}+\mathrm{Re}^{-1}\nabla_c^2\tilde{u}\\ -\partial P_1/\partial\bar{y}+\mathrm{Re}^{-1}\nabla_c^2\tilde{v}\end{pmatrix}, \tag{4.1b}$$

$$\nabla_c^2\equiv\frac{\partial^2}{\partial\bar{x}^2}+\frac{\partial^2}{\partial\bar{y}^2}, \tag{4.1c}$$

where $Re=v_nD/2\nu$. Equation (3.5a) and the boundary conditions (3.6) are unchanged. The above equations are solved numerically for both axisymmetric and planar geometries using Chebyshev spectral discretization along the normal to the wall. The steady-state solution is obtained by Newton iteration. Numerical solution leads not only to a description of the velocity field, but also to a description of the manner in which the pressure gradient C varies with Re, figure 2. Note that the large Re values are consistent with (3.7c), (3.9c). The small Reynolds number behaviour (deduced analytically) is

$$\left.\begin{aligned}C&=\frac{16}{Re}+12+O(Re)\ \text{(axisymmetric)},\\ C&=\frac{3}{Re}+\frac{81}{35}+O(Re)\ \text{(plane)},\end{aligned}\right\} \tag{4.2}$$

with corresponding velocity fields

$$\left.\begin{aligned}&\tilde{v}_r=(\bar{r}^3-2\bar{r}),\ \ \tilde{w}=4(1-\bar{r}^2)\ \text{(axisymmetric)},\\ &\tilde{v}=\tfrac{1}{2}(\bar{y}^3-3\bar{y}),\ \ \tilde{w}=\tfrac{3}{2}(1-\bar{y}^2)\ \text{(plane)}.\end{aligned}\right\} \tag{4.3}$$

(We are not suggesting that this limit is uniformly valid with respect to the small parameter D/L.)

There are *regular* viscous perturbations to the inviscid solutions (3.7), (3.9), relevant when Re is large, but we do not show them here.

Results intermediate between the limiting results (3.7), (3.9), (4.2) and (4.3) are shown in figures 3 and 4, from which it is clear that the inviscid limit provides

https://doi.org/10.1017/S0022112000002688 Published online by Cambridge University Press

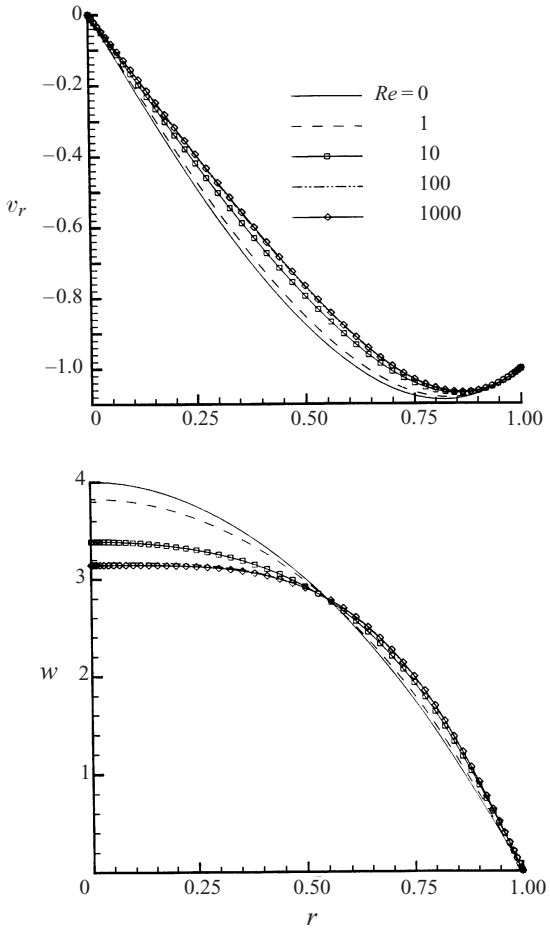


FIGURE 3. Axisymmetric viscous steady velocity field.

an accurate approximation for $Re > 100$. Note that in the plane case $\tilde{v}$ varies monotonically with $\bar{y}$ and is a maximum at the wall, whereas this is not the case for the axisymmetric problem.

Finite Reynolds number calculations for axisymmetric flows using a k–ϵ turbulence model have been reported by Sabnis, Giebling & McDonald (1989).

5. Perturbations of the circular-cylinder flow (linear analysis)

Consider a chamber whose cross-section is defined by

$$\bar{r} = 1 + \varepsilon R(\theta), \quad \varepsilon \ll 1. \tag{5.1}$$

We shall construct perturbations to the solution (3.7), generated in this way. Our analysis is also capable of accounting for perturbations generated in other ways, for example by variations in the injection speed v_n. Consider (3.5) and (3.6) dropping the tildes and overbars. We seek solutions

$$w = w_0 + \varepsilon w_1, \quad v_r = v_{r_0} + \varepsilon v_{r_1}, \quad v_\theta = \varepsilon v_{\theta_1}, \quad P_1 = p_0 + \varepsilon p_1, \quad \Omega = \varepsilon \Omega_1, \tag{5.2}$$

https://doi.org/10.1017/S0022112000002688 Published online by Cambridge University Press

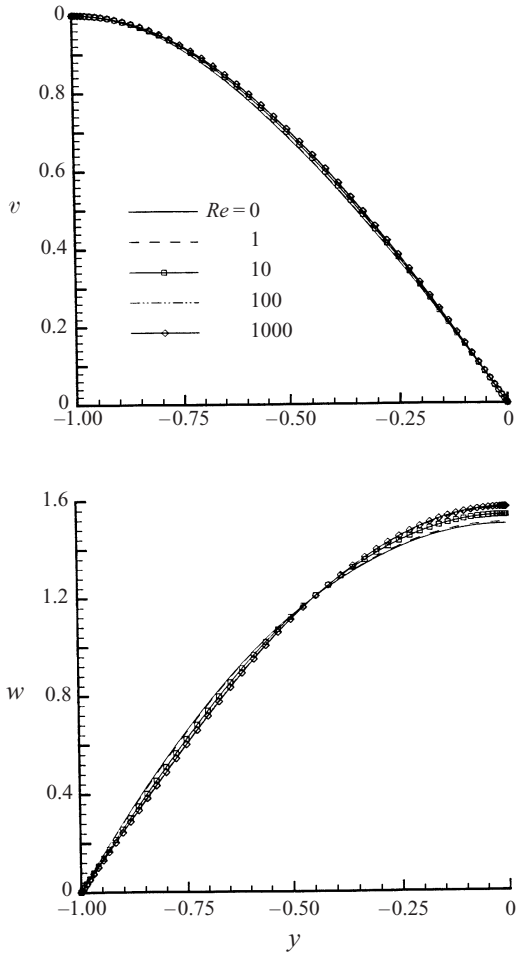


FIGURE 4. Plane viscous steady velocity field.

where Ω is the magnitude of the axial vorticity and v_{r_0}, w_0 is the solution (3.7). Since the axial vorticity transport equation is

$$(\hat{\boldsymbol{q}} \cdot \nabla)\Omega - w\Omega = 0, \quad \hat{\boldsymbol{q}} = (u, v, 0), \tag{5.3}$$

Ω_1 satisfies the equation

$$\frac{1}{\Omega_1}\frac{\partial \Omega_1}{\partial r} = -\pi r \cot\left(\tfrac{1}{2}\pi r^2\right), \tag{5.4}$$

whence

$$\Omega_1 \sin\left(\tfrac{1}{2}\pi r^2\right) = \text{const.} \tag{5.5}$$

It is tempting to eliminate the singular behaviour at $r = 0$ by setting the constant equal to 0 so that the perturbation cross-flow is a potential flow (albeit not harmonic, since it is not solenoidal). But in general such a flow cannot simultaneously satisfy the boundary conditions (3.6), and, as we have noted, this deficiency cannot be accommodated by placing a boundary layer at the wall, for such a boundary layer would necessarily be blown off. To regularize the solution, viscous terms must be retained and (4.1) must be considered. The viscous terms are important on the scale

https://doi.org/10.1017/S0022112000002688 Published online by Cambridge University Press

$r = O(1/\sqrt{Re})$ where $\Omega_1 = O(Re)$ so that the axial vorticity Ω is $O(\varepsilon Re)$. Thus the perturbations are only small everywhere if εRe is small. Later we shall relax this restriction, meantime noting that the linear analysis of this section is relevant to the larger context.

6. Solution of the vorticity equation

When $Re \gg 1$ the inviscid solution (5.5) is correct provided $r \gg 1/\sqrt{Re}$. Otherwise, Ω_1 satisfies the equation

$$-\frac{1}{r}\sin(\tfrac{1}{2}\pi r^2)\frac{\partial \Omega_1}{\partial r} = \pi\cos(\tfrac{1}{2}\pi r^2)\Omega_1 + \frac{1}{Re}\nabla^2\Omega_1 \tag{6.1}$$

which, in the viscous core $r = O(1/\sqrt{Re})$, can be approximated by

$$-\frac{\pi s}{2}\frac{\partial \Omega_1}{\partial s} = \pi\Omega_1 + \frac{\partial^2\Omega_1}{\partial s^2} + \frac{1}{s}\frac{\partial\Omega_1}{\partial s} - \frac{n^2}{s^2}\Omega_1, \tag{6.2}$$

where $s = r\sqrt{Re}$ and we have assumed an angular dependence $e^{in\theta}$ for some non-vanishing positive integer n. (The special and simple case $n = 0$ is discussed later.) Because the perturbations that we consider are of this nature, there are no perturbations to the constant C of (3.5*b*).

Solutions of (6.2) behave like $s^{\pm n}$ as $s \to 0$, and we define $H_n(s)$ to be the solution that satisfies the condition

$$\lim_{s\to 0} H_n s^{-n} = 1. \tag{6.3}$$

Also, H_n must behave like $1/s^2$ as $s \to \infty$ in order to match with the inviscid solution (5.5). The required solution is

$$H_n(s) = \frac{s^n \displaystyle\int_{-1/4}^{0} \mathrm{d}p\, e^{\pi p s^2}(-p)^{n/2}(1+4p)^{n/2-1}}{\displaystyle\int_{-1/4}^{0} \mathrm{d}p\,(-p)^{n/2}(1+4p)^{n/2-1}}, \tag{6.4}$$

which can be evaluated in terms of elementary functions when n is an even integer.

For large values of s,

$$H_n \sim \frac{\pi^{-1-n/2}\displaystyle\int_{-\infty}^{0} \mathrm{d}p\, e^{p}(-p)^{n/2}}{s^2\displaystyle\int_{-1/4}^{0} \mathrm{d}p\,(-p)^{n/2}(1+4p)^{n/2-1}} \equiv \frac{a}{s^2}. \tag{6.5}$$

Then if we write

$$\Omega_1 = A\,\mathrm{cosec}(\tfrac{1}{2}\pi r^2)e^{in\theta} \tag{6.6}$$

in the inviscid annulus (cf. (5.5)),

$$\Omega_1 = \frac{2ARe}{a\pi}H_n(s)e^{in\theta} \tag{6.7}$$

in the viscous core. These formulas provide a description of Ω_1 everywhere to within a constant (A). Graphs of $H_n(s)/a$ are shown in figure 5 for various values of n. H_n vanishes both on the axis and as $s \to \infty$, with a maximum at some finite value of s.

https://doi.org/10.1017/S0022112000002688 Published online by Cambridge University Press

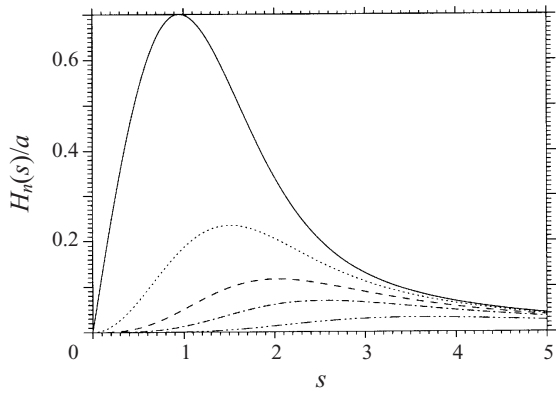


FIGURE 5. $H_n(s)/a$ against s for $n = 1$ (solid), $n = 2$ (dotted), $n = 3$ (dashed), $n = 4$ (dash-dot) and $n = 6$ (dash-dot-dot-dot).

As n increases the value of the maximum decreases, and its location shifts radially outwards.

7. The velocity field

The following estimates are valid within the viscous core:

$$v_{r1}, \quad v_{\theta 1} = O(\sqrt{Re}), \quad w_1 = O\left(\frac{1}{Re}\right), \quad \Omega_1 = O(Re). \tag{7.1a–c}$$

The first and third of these follow from the fact that Ω_1 is singular like $1/r^2$ in the inviscid annulus; the second follows from the fact that w_1 vanishes like r^2 in the annulus (see (8.5)). Then, to leading order within the core,

$$-\frac{1}{r}\frac{\partial}{\partial r}(rv_{\theta 1}) + \frac{1}{r}\frac{\partial v_{r1}}{\partial \theta} = \Omega_1, \quad \frac{\partial}{\partial r}(rv_{r1}) + \frac{\partial v_{\theta 1}}{\partial \theta} = 0, \tag{7.2}$$

so that a stream function may be defined ($v_{r1} = (1/r)\partial\psi/\partial\theta$, $v_{\theta 1} = -\partial\psi/\partial r$) and

$$\frac{\partial^2\psi}{\partial s^2} + \frac{1}{s}\frac{\partial\psi}{\partial s} - \frac{n^2}{s^2}\psi = \frac{2AH_n(s)}{a\pi}\mathrm{e}^{\mathrm{i}n\theta} \equiv f. \tag{7.3}$$

The solution that is regular at the origin is

$$\psi = C_1 s^n \mathrm{e}^{\mathrm{i}n\vartheta} + \frac{s^n}{2n}\int_0^s \mathrm{d}s\, f s^{-n+1} - \frac{s^{-n}}{2n}\int_0^s \mathrm{d}s f s^{n+1} \tag{7.4}$$

and we must choose $C_1 = -(1/2n)\int_0^\infty \mathrm{d}s\, \mathrm{e}^{-\mathrm{i}n\theta} f s^{-n+1}$ so that

$$\psi \sim \frac{-2A\mathrm{e}^{\mathrm{i}n\vartheta}}{\pi n^2}, \quad v_{r_1} \sim \frac{-2\mathrm{i}A\sqrt{Re}\mathrm{e}^{\mathrm{i}n\theta}}{\pi n s} \quad \text{as } s \to \infty. \tag{7.5a, b}$$

In the inviscid annulus v_{r_1} is singular like $1/r$, consistent with the $1/r^2$ singularity in Ω_1, and this behaviour matches (7.5*b*). We now turn to the solution in the inviscid annulus.

https://doi.org/10.1017/S0022112000002688 Published online by Cambridge University Press

8. The inviscid annulus, $1/\sqrt{Re} \ll r \leqslant 1$

Consider continuity, (3.5*a*), and the definition of Ω: these can be used to express v_{θ_1} and v_{r_1} in terms of Ω_1 and w_1. Thus

$$\frac{\mathrm{i}n}{r} v_{r_1} = \Omega_1 + \frac{\partial v_{\theta_1}}{\partial r} + \frac{1}{r} v_{\theta_1}, \tag{8.1}$$

and

$$v_{\theta_1} = r^{-1+n}\left[C_2 + \frac{1}{2n}\int_1^r \mathrm{d}r\, r^{2-n} g\right] + r^{-1-n}\left[v_{\theta_1}(1) - C_2 - \frac{1}{2n}\int_1^r \mathrm{d}r\, r^{2+n} g\right] \tag{8.2}$$

where

$$g \equiv \frac{-\mathrm{i}n w_1}{r} - \frac{1}{r^2}\frac{\partial}{\partial r}(r^2 \Omega_1) \tag{8.3}$$

and C_2 is determined by evaluating (8.1) at $r = 1$, whence

$$0 = \mathrm{i}n v_{r_1}(1) + n v_{\theta_1}(1) - A - 2nC_2. \tag{8.4}$$

In addition, the perturbed z-momentum equation, when solved for w_1, yields

$$w_1 = \sin^2\left(\frac{\pi r^2}{2}\right)\left[w_1(1) - \int_1^r \frac{\mathrm{d}r_1 v_{r_1} \pi^2 r^2}{\sin^2(\pi r^2/2)}\right], \tag{8.5}$$

from which we conclude that w_1 vanishes like r^2 as $r \to 0$ (cf. (7.1*b*)). Thus g vanishes like r as $r \to 0$, and with this information we can examine the small-r behaviour of v_{θ_1} from (8.2). Unacceptable singular behaviour (r^{-1-n}, which would imply improperly large values of $v_{\theta 1}$ in the viscous core) can only be eliminated if

$$v_{\theta_1}(1) - C_2 - \frac{1}{2n}\int_1^0 \mathrm{d}r\, r^{2+n} g = 0 \tag{8.6}$$

and this closes the problem and permits the evaluation of A, the vorticity amplitude (cf. (6.6)).

Solutions can be constructed in the following fashion: We guess w_1 and use (6.6), (8.4), (8.6) to calculate the constant A; v_{θ_1} is then determined from (8.2), followed by v_{r_1} from (8.1); and then a new estimate for w_1 follows from (8.5) and so on.

Boundary values at $r = 1$ must be assigned, and there are various possibilities. If the cross-section is unperturbed but the injection velocity is

$$v_n = 1 - \varepsilon \mathrm{e}^{\mathrm{i}n\theta} \tag{8.7}$$

then

$$v_{r_1}(1) = \mathrm{e}^{\mathrm{i}n\theta}, \quad v_{\theta_1}(1) = 0, \quad w_1(1) = 0. \tag{8.8}$$

If the injection velocity is fixed but the cross-section is perturbed, namely

$$r = 1 - \varepsilon \mathrm{e}^{\mathrm{i}n\theta}, \tag{8.9}$$

a shift in the boundary conditions (3.6) to $r = 1$ is equivalent to

$$v_{r_1}(1) = \mathrm{e}^{\mathrm{i}n\theta}, \quad v_{\theta_1}(1) = 0, \quad w_1(1) = -\pi^2 \mathrm{e}^{\mathrm{i}n\theta}. \tag{8.10}$$

In this case the lowest-order relevant mode corresponds to $n = 2$, as the case $n = 1$ is equivalent to mere displacement of the circular boundary without substantive effect on the flow field. Solutions for both these cases are shown in figures 6 and 7.

https://doi.org/10.1017/S0022112000002688 Published online by Cambridge University Press

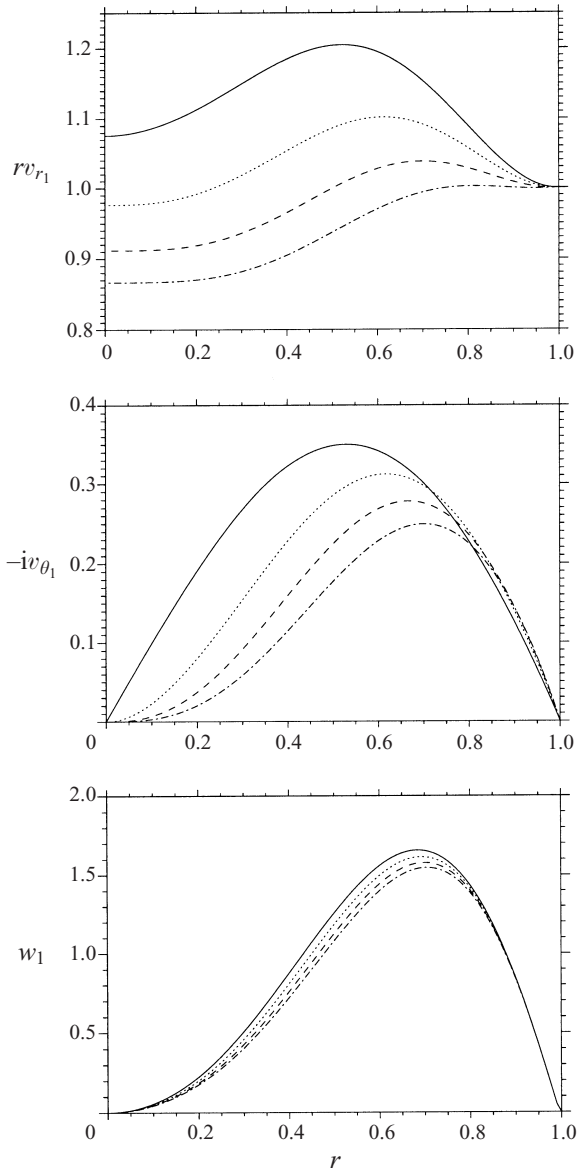


FIGURE 6. The behaviour of v_{r_1}, $-iv_{\theta_1}$ and w_1 in the inviscid annulus for the perturbed velocity problem with the modes $n = 2$ (solid lines, $\bar{A} = 3.397$), $n = 3$ (dotted lines, $\bar{A} = 4.6016$), $n = 4$ (dashed lines, $\bar{A} = 5.7285$) and $n = 5$ (dot-dash lines, $\bar{A} = 6.8061$). Here $A = i\bar{A}$.

Note that in this section we have calculated perturbations that are linear in ϵ and have azimuthal variations $\sim e^{in\theta}$. Additional axisymmetric perturbations can be calulated, some of which are proportional to $1/Re$ (viscous corrections to the Culick solution), and some of which are small because D/L is small (corrections to the asymptotic description that satisfies (3.5)). No assumptions need be made about the relative magnitude of these various terms in this linear context, and those that we have calculated are distinguished from the others by their azimuthal variations and by the swirl.

https://doi.org/10.1017/S0022112000002688 Published online by Cambridge University Press

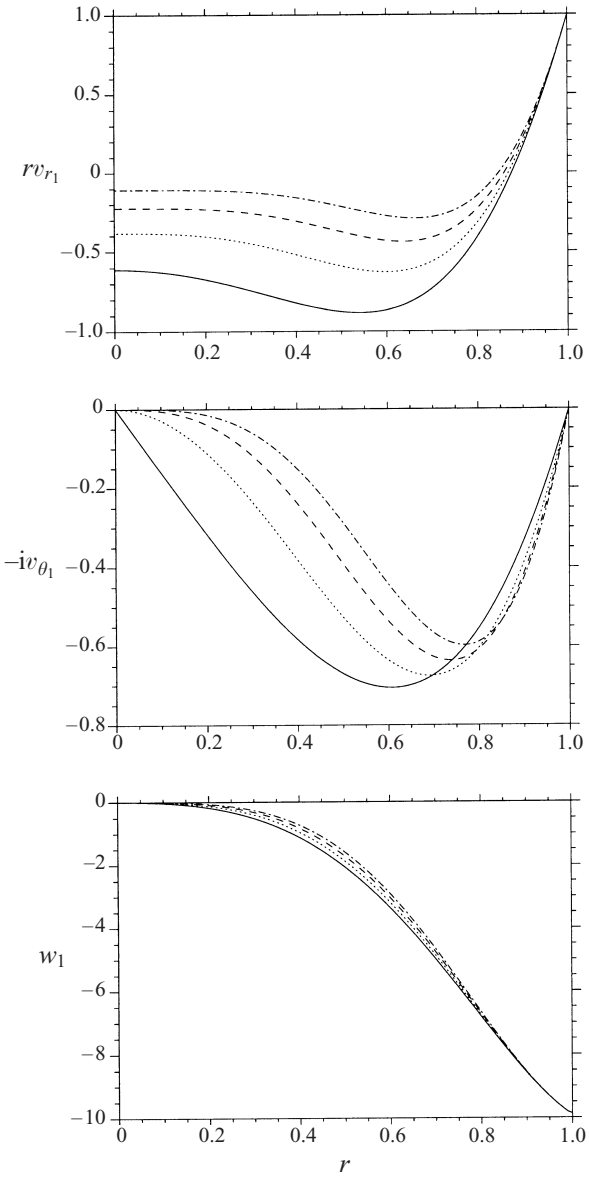


FIGURE 7. The behaviour of v_{r_1}, $-iv_{\theta_1}$ and w_1 in the inviscid annulus for the perturbed cylinder problem with the modes $n = 2$ (solid lines, $\bar{A} = -1.9245$), $n = 3$ (dotted lines, $\bar{A} = -1.8067$), $n = 4$ (dashed lines, $\bar{A} = -1.4102$) and $n = 5$ (dot-dash lines, $\bar{A} = -0.8467$). Here $A = i\bar{A}$.

9. Numerical solution of the linear problem

In addition to the asymptotic treatment, we have calculated the small-perturbation solutions by numerically solving the linearized equations for finite Reynolds numbers. The numerical procedure is similar to what we describe in § 10, sans iterations. Care is required in guaranteeing proper behaviour of the solution in the neighbourhood of

https://doi.org/10.1017/S0022112000002688 Published online by Cambridge University Press

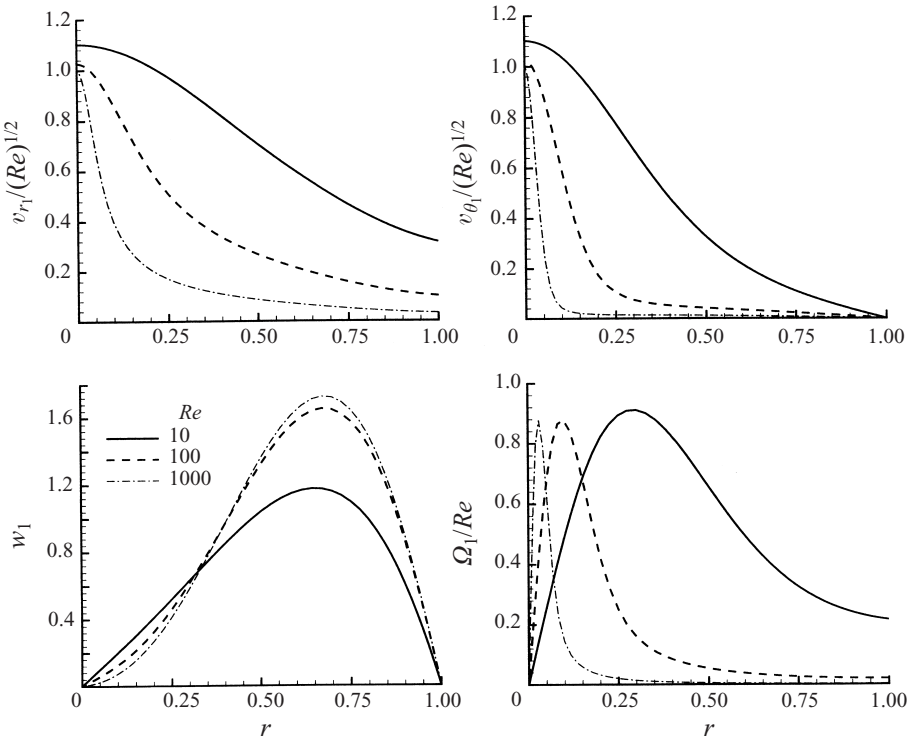


FIGURE 8. Perturbation solution when the injection velocity is perturbed, $n = 1$.

the origin. For the velocity components to be analytic there, we require, as $r \to 0$,

$$v_{r1} \to \begin{cases} b_o r & \text{for } n = 0 \\ b_n r^{n-1} & \text{for } n \neq 0, \end{cases} \tag{9.1a}$$

$$v_{\theta 1} \to \begin{cases} c_o r & \text{for } n = 0 \\ i b_n r^{n-1} & \text{for } n \neq 0, \end{cases} \tag{9.1b}$$

$$w_1 \to d_n r^n \quad \text{for all } n, \tag{9.1c}$$

for certain constants b_j, c_j, d_j. This behaviour is consistent with the vorticity vanishing as r^n.

Figures 8–10 show the vorticity and velocity perturbations generated by the injection perturbation (8.7) for $n = 1, 2, 3$, and several values of Re. The asymptotic conclusions $v_{r_1},\ v_{\theta_1} = O(\sqrt{Re})$, $w_1 = O(1/Re)$, $\Omega_1 = O(Re)$ within the viscous core of diameter $O(1/\sqrt{Re})$ are clearly evident in these figures. The radial velocity shows $1/r$ behaviour and the axial vorticity shows $1/r^2$ behaviour within the inviscid annulus, singular behaviour as the origin is approached that is regularized within the viscous core. The *intensity* of the viscous core, measured both by the magnitude of the perturbations within it and its narrowness, decreases with increasing mode number. Note that $v_{\theta 1}$ and v_{r1} do not vanish at $r = 0$ when $n = 1$, but do vanish there when $n \neq 1$, behaviour noted in the context of jet flows by Batchelor & Gill (1962).

Figures 11 and 12 show the corresponding results for $n = 2$ and $n = 3$ when the cross-section is perturbed with the injection velocity fixed, (8.9).

https://doi.org/10.1017/S0022112000002688 Published online by Cambridge University Press

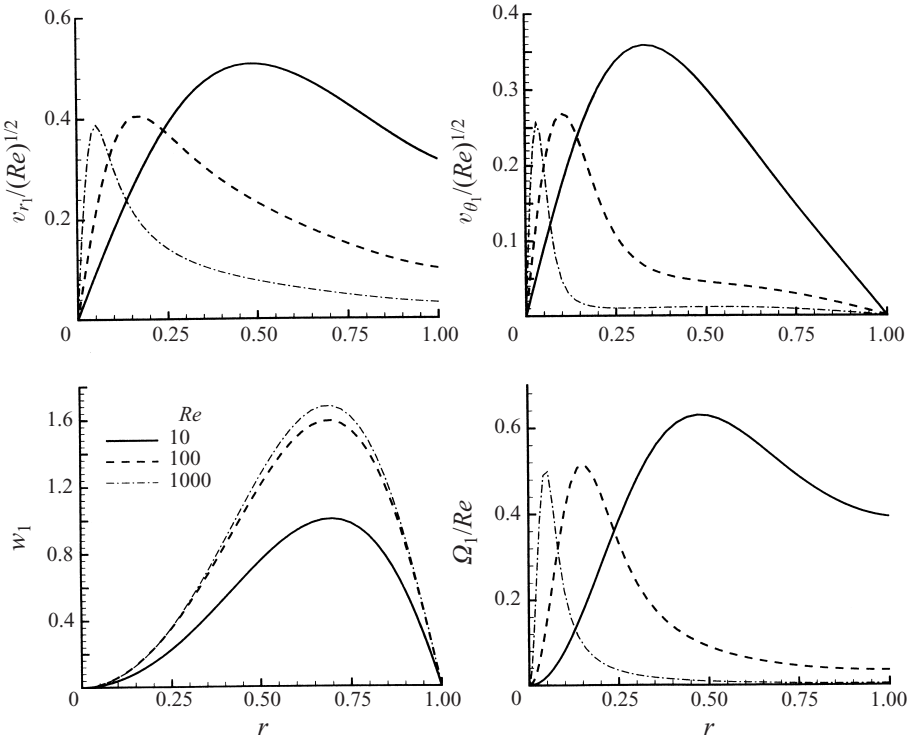


FIGURE 9. Perturbation solution when the injection velocity is perturbed, $n = 2$.

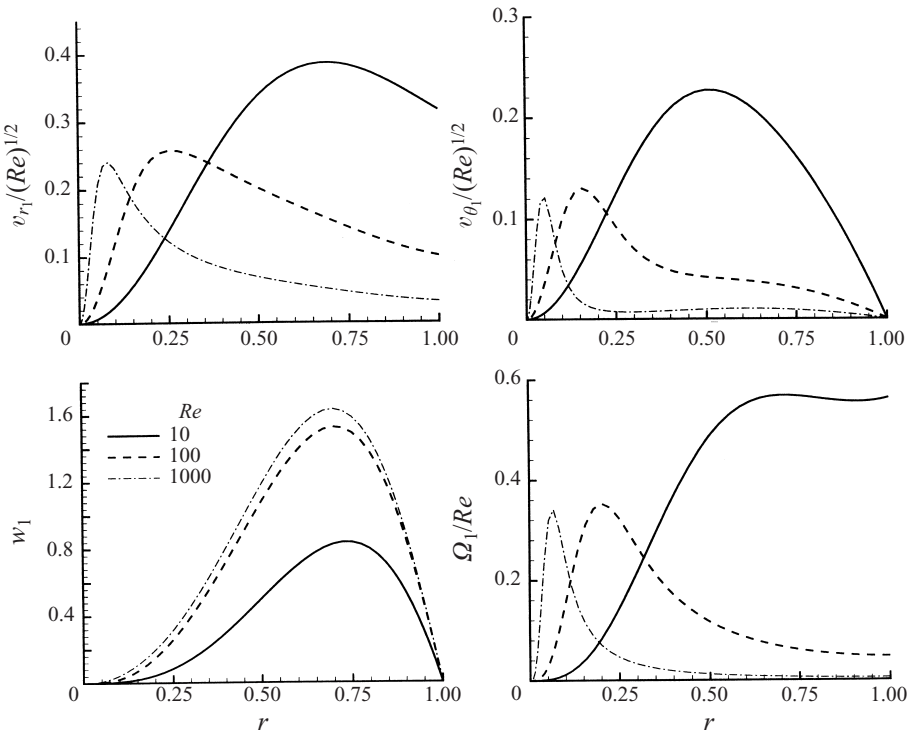


FIGURE 10. Perturbation solution when the injection velocity is perturbed, $n = 3$.

https://doi.org/10.1017/S0022112000002688 Published online by Cambridge University Press

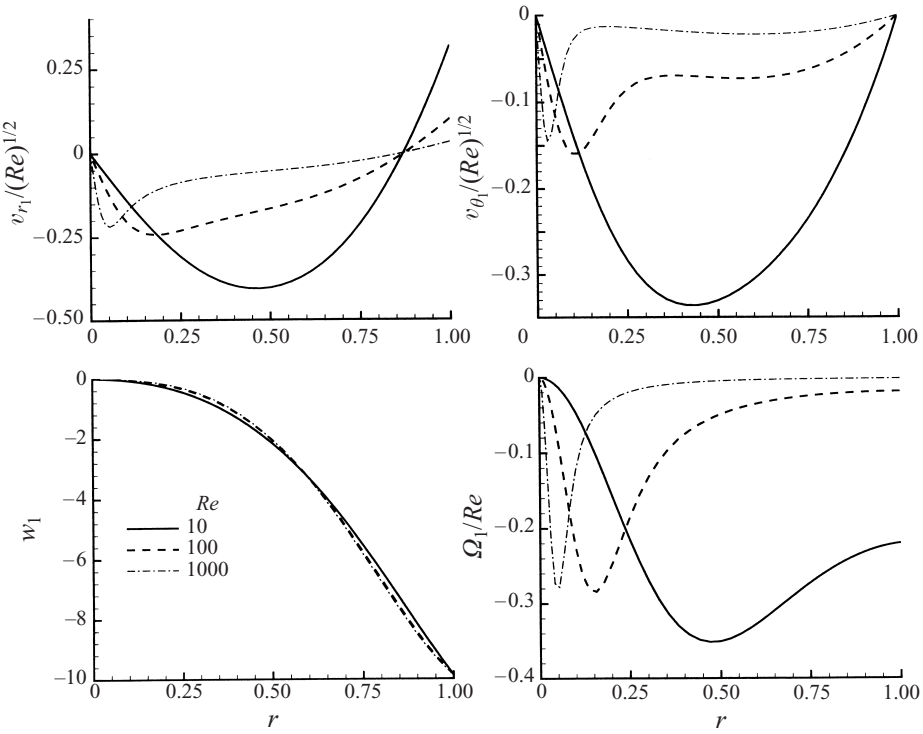


FIGURE 11. Perturbation solution when the radius is perturbed, $n = 2$.

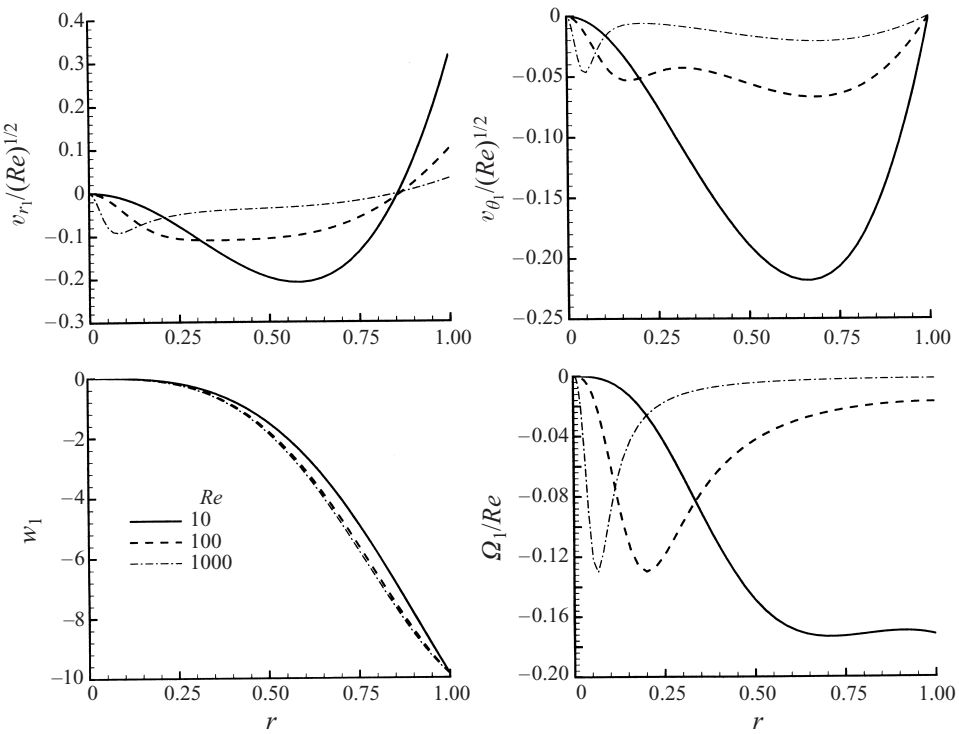


FIGURE 12. Perturbation solution when the radius is perturbed, $n = 3$.

https://doi.org/10.1017/S0022112000002688 Published online by Cambridge University Press

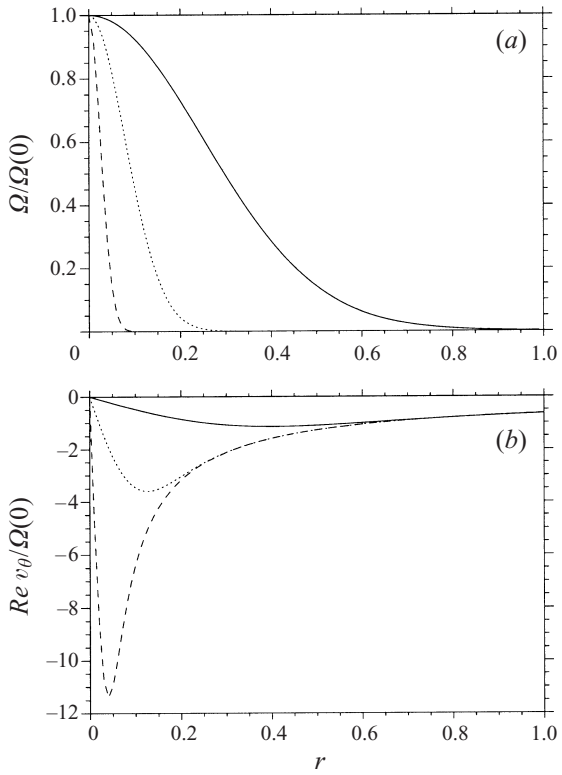


FIGURE 13. (*a*) Axial vorticity against r and (*b*) circumferential velocity against r for $Re = 10$ (solid), $Re = 100$ (dotted) and $Re = 1000$ (dashed), $n = 0$.

9.1. *The case* $n = 0$

Here an exact solution can be constructed without approximation, since v_θ and Ω satisfy the equations

$$\left.\begin{aligned} v_{r0}\frac{\partial \Omega}{\partial r} - w_0\Omega &= \frac{1}{Re}\frac{1}{r^2}\frac{\partial}{\partial r}\left(r\frac{\partial \Omega}{\partial r}\right), \\ \Omega &= -\frac{1}{r}\frac{\partial}{\partial r}(rv_\theta), \end{aligned}\right\} \tag{9.2}$$

Thus

$$\frac{\Omega}{\Omega(0)} = \exp\left[-Re\int_0^r \frac{\mathrm{d}r}{r}\sin\left(\tfrac{1}{2}\pi r^2\right)\right] = \exp\left[-\tfrac{1}{2}Re\,\mathrm{Si}\left(\tfrac{1}{2}\pi r^2\right)\right] \tag{9.3}$$

(see figure 13*a*) which behaves like

$$\exp\left(-\tfrac{1}{4}\pi s^2\right) \equiv H_0(s) \tag{9.4}$$

in the viscous core when Re is large, and is exponentially small in the inviscid annulus. Here $\mathrm{Si}(x)$ is the Sine Integral; v_θ is obtained by quadrature, figure 13(*b*), and for large Re has the uniformly valid representation

$$\frac{Re}{\Omega(0)}v_\theta \sim -\frac{2}{\pi}\frac{\sqrt{Re}}{s}\left[1 - \mathrm{e}^{-\pi s^2/4}\right] \tag{9.5}$$

which behaves like $-2/\pi r$ in the inviscid annulus.

https://doi.org/10.1017/S0022112000002688 Published online by Cambridge University Press

10. Solution when $\varepsilon \ll 1$ and $\varepsilon \gg 1/Re$ or $\varepsilon = O(1/Re)$

The linear analysis ($n \neq 0$) of the previous sections is of little if any practical interest when applied everywhere in the chamber, since the applied perturbations must necessarily be very small for realistic values of the Reynolds number. And so in this section we consider larger perturbations for which part of the perturbation flow field is nonlinear. With the earlier analysis this constitutes a complete description when $\varepsilon \ll 1$, for any value of Re.

The linear analysis is still correct when $r = O(1)$ and our starting point is the small-r behaviour:

$$\Omega \sim \frac{\varepsilon 2A\mathrm{e}^{\mathrm{i}n\theta}}{\pi r^2} \quad \text{(see (6.6))}, \tag{10.1}$$

$$\varepsilon v_{r_1} \sim \frac{-\varepsilon \mathrm{i} 2A\mathrm{e}^{\mathrm{i}n\vartheta}}{n\pi r} \tag{10.2}$$

(from (8.1), noting that v_{θ_1} vanishes at least as rapidly as r);

$$v_{r_0} \sim -\tfrac{1}{2}\pi r, \quad w \sim \pi. \tag{10.3}$$

From these it is apparent that v_{r_0} and εv_{r_1} are comparable when $r = O(\sqrt{\varepsilon})$. On this scale there is a nonlinear description in which

$$\Omega, w = O(1), \quad v_r,\ v_\theta = O(\sqrt{\varepsilon}). \tag{10.4}$$

We shall call this region the *nonlinear patch*. When $\varepsilon Re = O(1)$, viscous terms are important on the same scale; when $\varepsilon Re \gg 1$, viscous terms are only important on a smaller scale, defining a viscous core.

In the scaled variables appropriate for the nonlinear patch ($r = \sqrt{\varepsilon} r^+$, etc.) we have

$$\Omega^+ = \frac{1}{r^+}\frac{\partial v_r^+}{\partial \theta} - \frac{1}{r^+}\frac{\partial}{\partial r^+}(r^+ v_\theta^+), \tag{10.5a}$$

$$u^+\frac{\partial w^+}{\partial x^+} + v^+\frac{\partial w^+}{\partial y^+} + w^{+2} = \pi^2, \tag{10.5b}$$

$$\frac{1}{r^+}\frac{\partial}{\partial r^+}(r^+ v_r^+) + \frac{1}{r^+}\frac{\partial v_\theta^+}{\partial \theta} + w^+ = 0, \tag{10.5c}$$

$$v_r^+\frac{\partial \Omega^+}{\partial r^+} + \frac{v_\theta^+}{r^+}\frac{\partial \Omega^+}{\partial \theta} = w^+\Omega^+ + \frac{1}{\varepsilon Re}\nabla^{+2}\Omega^+. \tag{10.5d}$$

The appropriate solution of (10.5*b*) is

$$w^+ = \pi. \tag{10.6}$$

Then, writing

$$v_r^+ = -\tfrac{1}{2}\pi r^+ + V_r^+, \tag{10.7}$$

continuity, (10.5*c*), becomes

$$\frac{1}{r^+}\frac{\partial}{\partial r^+}(r^+ V_r^+) + \frac{1}{r^+}\frac{\partial v_\theta^+}{\partial \theta} = 0 \tag{10.8}$$

which can be satisfied by the introduction of the stream function Ψ^+, namely

$$V_r^+ = \frac{1}{r^+}\frac{\partial \Psi^+}{\partial \theta}, \quad v_\theta^+ = -\frac{\partial \Psi^+}{\partial r^+}, \tag{10.9}$$

https://doi.org/10.1017/S0022112000002688 Published online by Cambridge University Press

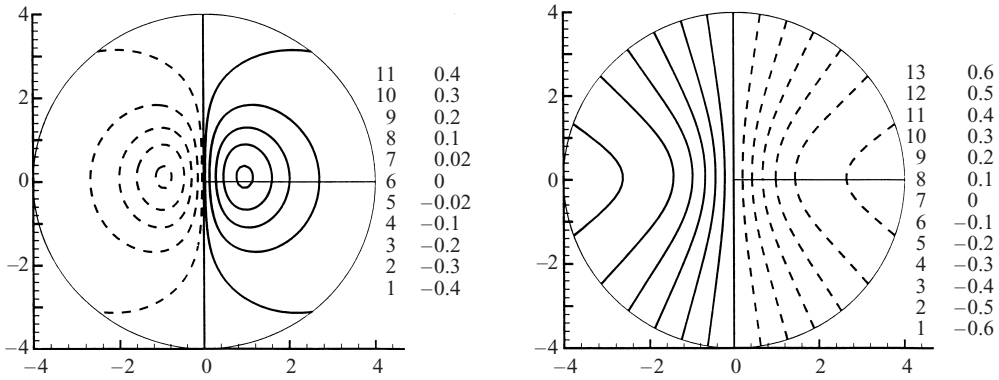


FIGURE 14. Contours of vorticity (left) and stream function (right) for $n = 1$ and $\varepsilon Re = 1.0$.

whence

$$\Omega^+ = \nabla^{+2}\Psi^+. \tag{10.10}$$

The vorticity transport equation becomes

$$\left(-\tfrac{1}{2}\pi r^+ + \frac{1}{r^+}\frac{\partial \Psi^+}{\partial \theta}\right)\frac{\partial \Omega^+}{\partial r^+} - \frac{1}{r^+}\frac{\partial \Psi^+}{\partial r^+}\frac{\partial \Omega^+}{\partial \theta} = \pi\Omega^+ + \frac{1}{\varepsilon Re}\nabla^{+2}\Omega^+. \tag{10.11}$$

Matching conditions as $r^+ \to \infty$ are defined by (10.2), (10.3). More precisely, any linear perturbation in the core can be expressed as a Fourier sum of terms of this kind. We shall restrict attention to a single mode, with

$$\Psi^+ \to \frac{-2}{n^2\pi}\cos(n\theta), \quad \Omega^+ \sim \frac{2}{\pi r^{+2}}\cos(n\theta) \quad \text{as } r^+ \to \infty, \tag{10.12}$$

corresponding to the small-r linear description

$$v_r \sim -\tfrac{1}{2}\pi r + \frac{\varepsilon 2}{n\pi r}\sin(n\theta), \quad \Omega \sim \frac{\varepsilon 2\cos(n\theta)}{\pi r^2}. \tag{10.13}$$

We have chosen $A = 1$ (without loss of generality) since it can be absorbed into ε.

Equations (10.10), (10.11) are solved numerically, subject to the boundary conditions (10.12), using spectral methods for various values of εRe and n. A Fourier Galerkin scheme is used along the circumferential direction and Chebyshev collocation is used along the radial direction. With increasing εRe, the effect of nonlinearity increases and correspondingly the resolution requirement also increases. The results to be presented below are obtained using a 21-mode expansion along the circumferential direction, and 51 points along the radial direction. This resolution was found to be adequate over the range of εRe considered here. Solutions for Ψ^+ and Ω^+ were obtained through Newton iteration. As $r \to 0$ appropriate decay is required of both vorticity and stream function consistent with the analytical behaviour for velocity given in (9.1). Such accurate description of the solution near the origin is important for rapid convergence of the iterative procedure. For all cases considered rapid convergence is obtained within about ten iterations. For computational purposes the outer boundary is chosen to be finite and the results to be presented below are for $r^+ = 4$. Numerical sensitivity of the results to the placement of the outer boundary has been verified to be minimal.

Figure 14 shows contours of vorticity and stream function plotted for the case $n = 1$ and εRe=1. The vorticity exhibits a dipole-like pattern with a peak vorticity magnitude

https://doi.org/10.1017/S0022112000002688 Published online by Cambridge University Press

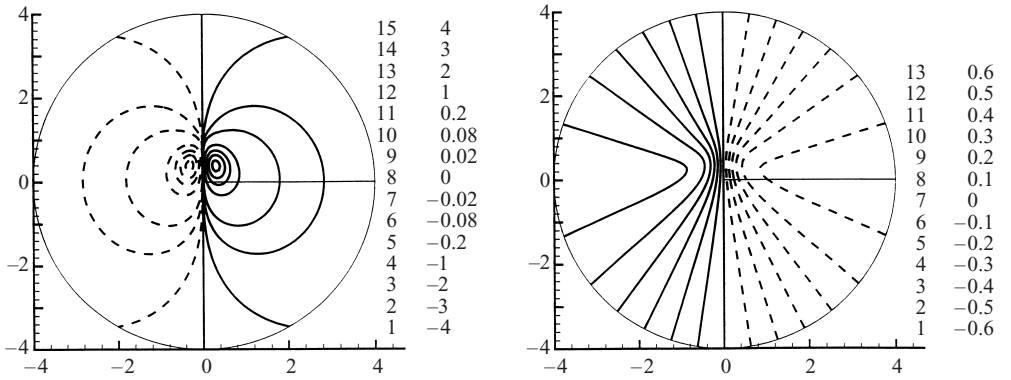


FIGURE 15. Contours of vorticity and stream function for $n = 1$ and $\varepsilon Re = 10.0$.

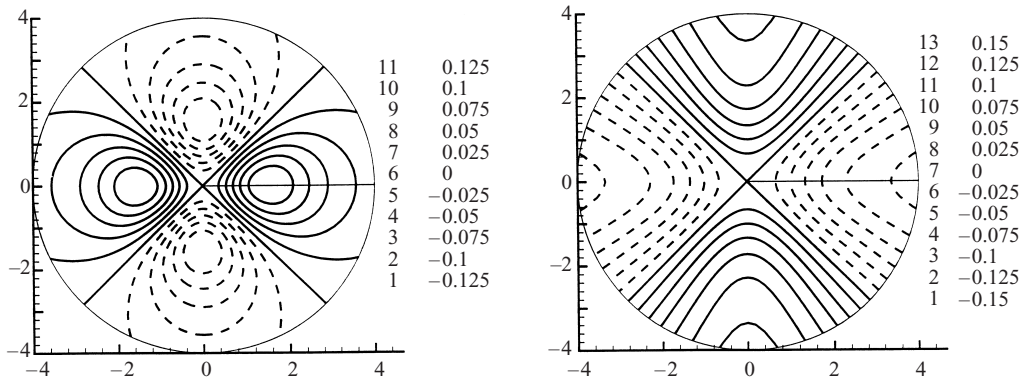


FIGURE 16. Contours of vorticity and stream function for $n = 2$ and $\varepsilon Re = 1.0$.

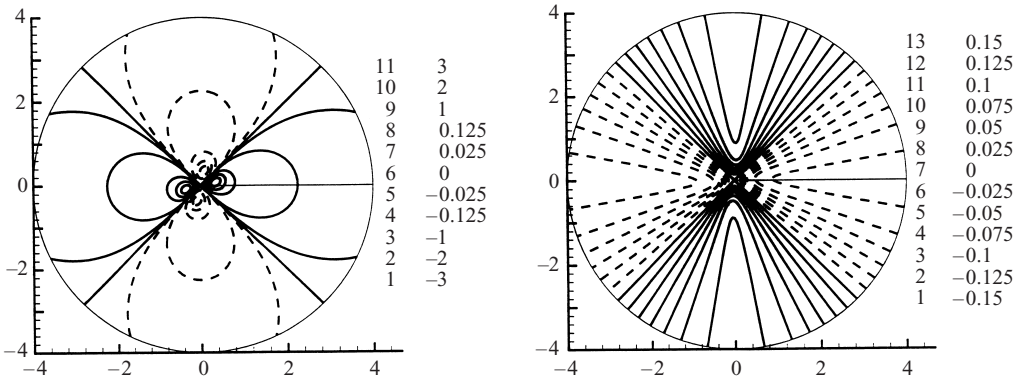


FIGURE 17. Contours of vorticity and stream function for $n = 2$ and $\varepsilon Re = 25.0$.

of approximately 0.416 at $r \approx 0.92$. As εRe increases, the vorticity maximum increases (see figure 15 for $\varepsilon Re = 10$) and the top–bottom symmetry of the pattern is further destroyed. At small εRe the vorticity peaks are separated by 180°. With increasing nonlinearity, the phase relation of the higher circumferential harmonics is such that the angular separation of the points of peak vorticity decreases. The radial location of peak vorticity draws closer to the origin.

https://doi.org/10.1017/S0022112000002688 Published online by Cambridge University Press

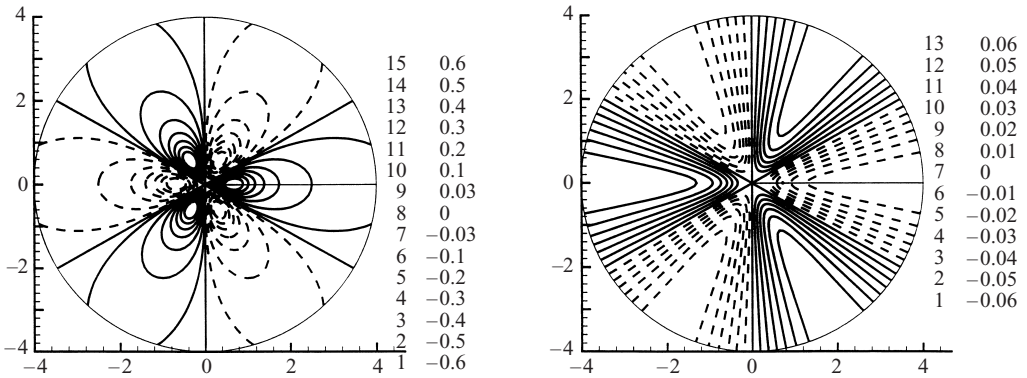


FIGURE 18. Contours of vorticity and stream function for $n = 3$ and $\varepsilon Re = 10.0$.

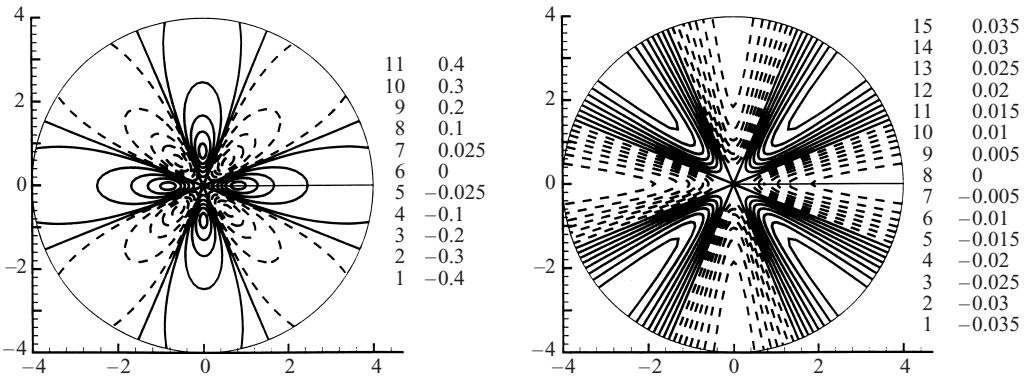


FIGURE 19. Contours of vorticity and stream function for $n = 4$ and $\varepsilon Re = 10.0$.

Figure 16 shows the vorticity and stream function contours for the case $n = 2$, $\varepsilon Re = 1$. The vorticity distribution exhibits a quadrapole pattern with the peak vorticity substantially less than that for $n = 1$, figure 14. With increasing εRe (see figure 17 for $\varepsilon Re = 25$) the pattern is distorted and the peak vorticity occurs closer to the origin. Figures 18 and 19 show the solutions for $n = 3$ and $n = 4$, revealing sextapole and octapole patterns. The maximum vorticity progressively decreases with n, and the symmetry is destroyed with increasing Reynolds number. Figure 20 shows near-origin views of the velocity vector plot (V_r^+, v_θ^+) for the four cases $n = 1, 2, 3, 4$, at $\varepsilon Re = 25$.

The scaling of maximum vorticity with Reynolds number is shown in figure 21. A near linear scaling of the form $\Omega_{peak}^+ = c\varepsilon Re$ is observed with the coefficient c taking values 0.424, 0.147, 0.074, and 0.043 when $n = 1, 2, 3, 4$. The radial location of the vorticity peak is shown in figure 22(a). With increasing εRe the axial vortices first move rapidly towards the origin, but then move away. This behaviour can be seen in the $n = 1, 2$ cases and is probably a feature of the solutions for larger n at sufficiently large Reynolds numbers. Finally we quantify the distortion from the regular pole patterns in terms of the smallest angular separation between two adjacent vorticity peaks (see figure 22b). For vanishing Reynolds number, the separation is $180/n^\circ$. The effect of the nonlinearity is significant for $n = 1, 2$ at the Reynolds numbers we have considered.

https://doi.org/10.1017/S0022112000002688 Published online by Cambridge University Press

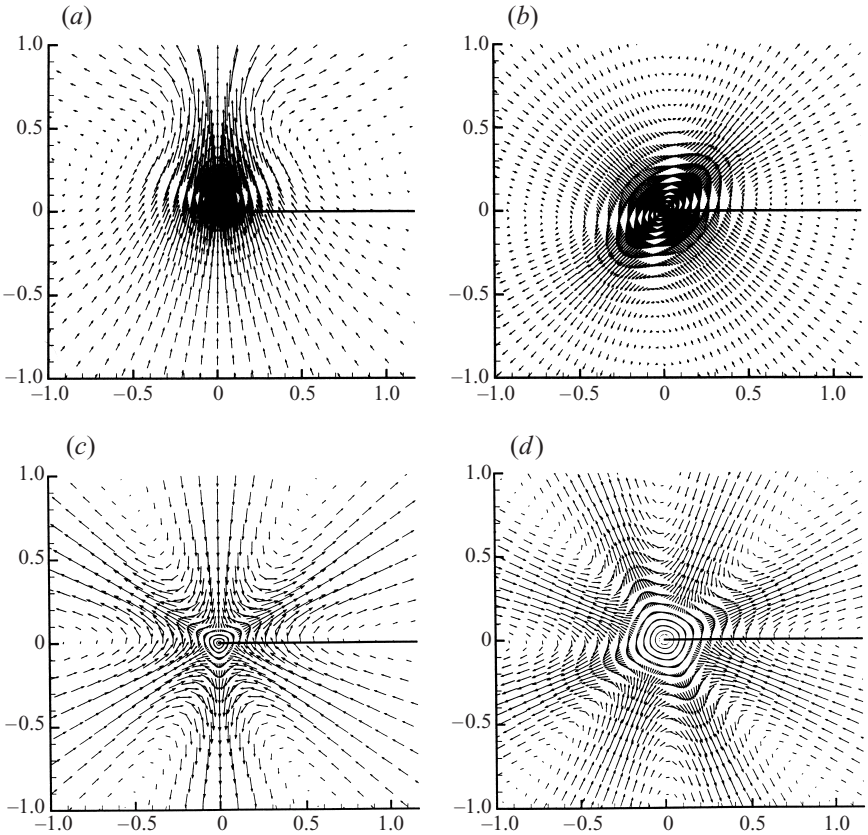


FIGURE 20. Velocity vectors for $\varepsilon Re = 10.0$: (*a*) $n = 1$, (*b*) $n = 2$, (*c*) $n = 3$, (*d*) $n = 4$.

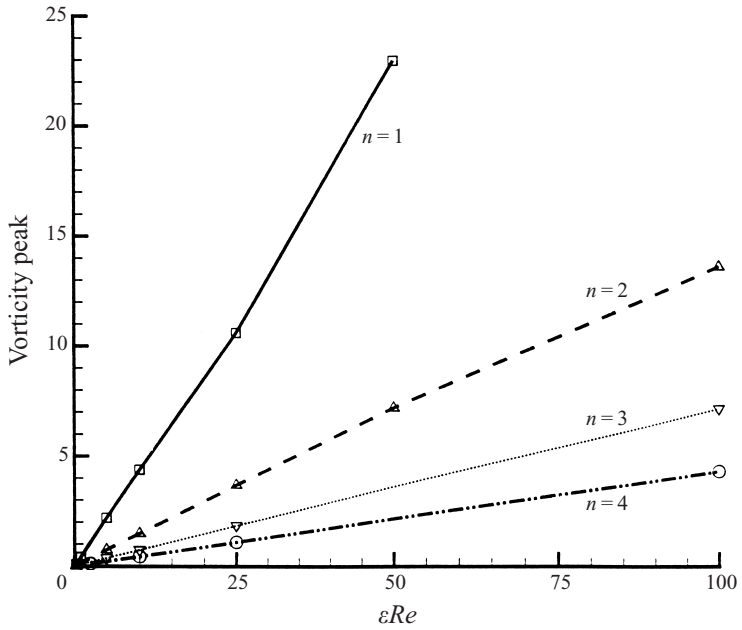


FIGURE 21. The scaling of maximum vorticity with Reynolds number.

https://doi.org/10.1017/S0022112000002688 Published online by Cambridge University Press

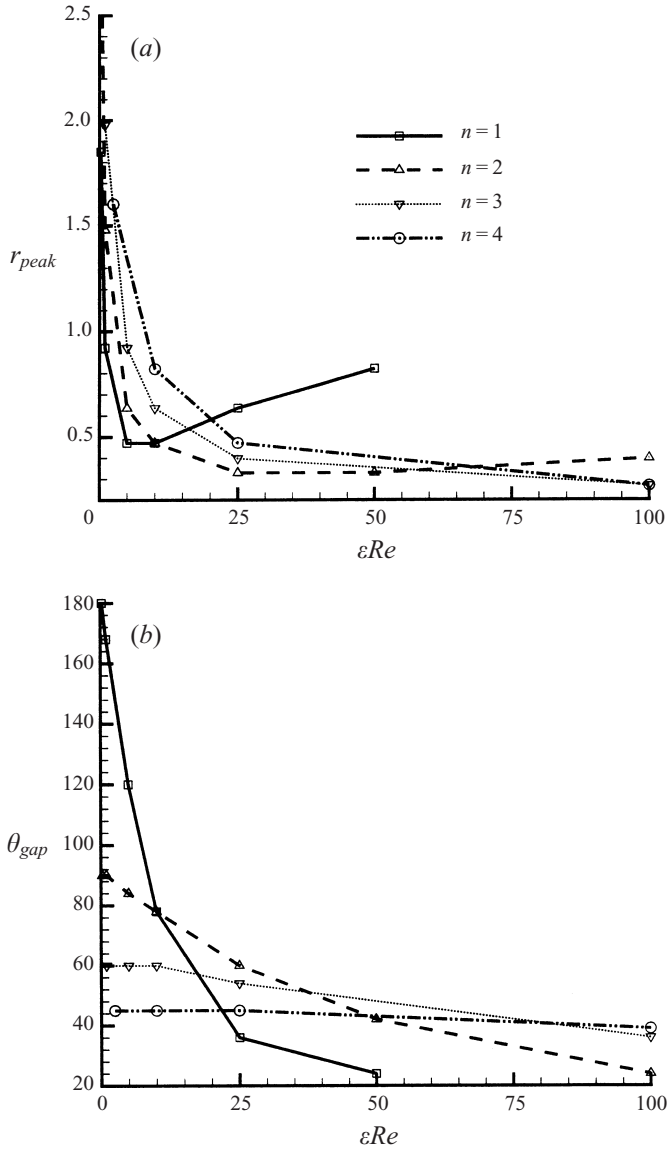


FIGURE 22. (*a*) The radial location of the vorticity peak, and (*b*) the angular separation between two vorticity peaks, as a function of Reynolds number.

11. Concluding remarks

Our main conclusions can be summarized succintly. Small deviations from axial symmetry in a solid-propellant rocket-motor flow lead to large values of axial vorticity, and to failure of the inviscid solution near the centreline. Our results make clear that, in numerical simulations, mesh points must be concentrated in a neighbourhood of the centreline, and this will be true not only for the laminar flows that we have considered, but also for large-eddy simulations of turbulent flows, a subject of great interest at the present time. The mechanisms that are responsible for this are straightforward, analogous to those that create a bath-tub vortex, but do not appear to have been considered before.

https://doi.org/10.1017/S0022112000002688 Published online by Cambridge University Press

Experimental manifestation of swirl generation, albeit unexplained, is reported in Dunlap *et al.* (1990). In the cold-flow simulations of that study, a significant circumferential velocity field was observed, although the chamber was nominally symmetric. This is indicated schematically (Dunlap *et al.* 2000, figure 6) as a simple swirling flow ($n = 0$), but the velocity was only measured in a single longitudinal plane, and so such measurements cannot distinguish $n = 0$ swirl from $n = 2, 4, \ldots$ swirl.

The response of the flow field to a small disturbance of increasing amplitude is not conventional. Very small disturbances, those for which εRe is small, give rise to a linear response everywhere. But this does not grow uniformly as ε is increased until a nonlinear description prevails. Instead, a domain of radius $O(\sqrt{\varepsilon})$ develops in the neighbourhood of the centreline within which the response is $O(1)$, outside of which it remains small. Ultimately the response everywhere in the chamber becomes nonlinear because of the growth of this domain, the nonlinear patch.

This work was supported by AFOSR (JB, MS) and by the U.S. Department of Energy through the University of California under Subcontract number B341494 (JB, MS, SB).

REFERENCES

Balakrishnan, G., Liñán, A. & Williams, F. A. 1991 Compressibility effects in thin channels with injection. *AIAA J.* **29**, 2149–2154.

Balakrishnan, G., Liñán, A. & Williams, F. A. 1992 Rotational inviscid flow in laterally burning solid-propellant rocket motors. *J. Propulsion Power* **8**, 1167–1176.

Batchelor, G. K. 1967 *An Introduction to Fluid Dynamics*. Cambridge University Press.

Batchelor, G. K. & Gill, A. E. 1962 Analysis of the stability of axisymmetric jets. *J. Fluid Mech.* **14**, 529–551.

Cole, J. D. & Aroesty, J. 1968 The blowhard problem – inviscid flows with surface injection. *Intl J. Heat Mass Transfer* **11**, 1167–1183.

Culick, F. E. C. 1966 Rotational axisymmetric mean flow and damping of acoustic waves in solid propellant rocket motors. *AIAA J.* **4**, 1462–1464.

Dunlap, R., Blackner, A. M., Waugh, R. C., Brown, R. S. & Willoughby, P. G. 1990 Internal flow field studies in a simulated cylindrical port rocket chamber. *J. Propulsion* **6**, 690–704.

Sabnis, J. S., Giebling, H. J. & McDonald, H. M. 1989 Navier–Stokes analysis of solid propellant rocket motor internal flows. *J. Propulsion Power* **5**, 657–664.

Sutton, G. 1992 *Rocket Propulsion Elements*, 6th Edn, John Wiley & Sons.

Taylor, G. I. 1956 Fluid flow in regions bounded by porous surfaces. *Proc. R. Soc. Lond.* A **234**, 456–475.

https://doi.org/10.1017/S0022112000002688 Published online by Cambridge University Press